Monochromatic backlighting of direct-drive cryogenic DT implosions on OMEGA

C. Stoeckl, R. Epstein, R. Betti, W. Bittle, J. A. Delettrez, C. J. Forrest, V. Yu. Glebov, V. N. Goncharov, D. R. Harding, I. V. Igumenshchev, D. W. Jacobs-Perkins, R. T. Janezic, J. H. Kelly, T. Z. Kosc, R. L. McCrory, D. T. Michel, C. Mileham, P. W. McKenty, F. J. Marshall, S. F. B. Morse, S. P. Regan, P. B. Radha, B. Rice, T. C. Sangster, M. J. ShoupIII, W. T. Shmayda, C. Sorce, W. Theobald, J. Ulreich, M. D. Wittman, D. D. Meyerhofer, J. A. Frenje, M. Gatu Johnson, and R. D. Petrasso

Citation: Physics of Plasmas **24**, 056304 (2017); doi: 10.1063/1.4977918
View online: http://dx.doi.org/10.1063/1.4977918
View Table of Contents: http://aip.scitation.org/toc/php/24/5
Published by the American Institute of Physics

Monochromatic backlighting of direct-drive cryogenic DT implosions on OMEGA

C. Stoeckl,[1,a)] R. Epstein,[1] R. Betti,[1] W. Bittle,[1] J. A. Delettrez,[1] C. J. Forrest,[1] V. Yu. Glebov,[1] V. N. Goncharov,[1] D. R. Harding,[1] I. V. Igumenshchev,[1] D. W. Jacobs-Perkins,[1] R. T. Janezic,[1] J. H. Kelly,[1] T. Z. Kosc,[1] R. L. McCrory,[1] D. T. Michel,[1] C. Mileham,[1] P. W. McKenty,[1] F. J. Marshall,[1] S. F. B. Morse,[1] S. P. Regan,[1] P. B. Radha,[1] B. Rice,[1] T. C. Sangster,[1] M. J. Shoup III,[1] W. T. Shmayda,[1] C. Sorce,[1] W. Theobald,[1] J. Ulreich,[1] M. D. Wittman,[1] D. D. Meyerhofer,[2] J. A. Frenje,[3] M. Gatu Johnson,[3] and R. D. Petrasso[3]

[1]*Laboratory for Laser Energetics, University of Rochester, 250 East River Road, Rochester, New York 14623-1299, USA*
[2]*Los Alamos National Laboratory Los Alamos, New Mexico 87545, USA*
[3]*Plasma Science Fusion Center Massachusetts Institute of Technology Cambridge, Massachusetts 02139, USA*

(Received 13 December 2016; accepted 30 January 2017; published online 13 March 2017)

Backlighting is a powerful technique to observe the flow of cold and dense material in high-energy-density–plasma experiments. High-performance, direct-drive cryogenic deuterium–tritium (DT) implosions are a challenging backlighting configuration because of the low opacity of the DT shell, the high shell velocity, the small size of the stagnating shell, and the very bright self-emission of the hot core. A crystal imaging system with a Si He_α backlighter at 1.865 keV driven by ~20-ps short pulses from OMEGA EP was developed to radiograph the OMEGA cryogenic implosions. The high throughput of the crystal imaging system makes it possible to record high-quality images with good photon statistics and a spatial resolution of ~15 μm at 10% to 90% modulation. This imager has been used to study the evolution of preimposed mass-density perturbations in the ablator, to quantify the perturbations caused by the stalk that is used to mount the target, and to study the mix caused by laser imprint or small-scale debris on the target surface. Because of the very low opacity of DT relative to carbon, even 0.1% of mix of carbon into the DT ice can be reliably inferred from the images. With the current implosion designs, mix is only observed for an adiabat below $\alpha = 4$. *Published by AIP Publishing.* [http://dx.doi.org/10.1063/1.4977918]

I. INTRODUCTION

Layered cryogenic deuterium–tritium (DT) targets are the baseline approach for achieving ignition in direct-drive inertial confinement fusion (ICF) experiments.[1,2] A steady progress has been made in experiments with hydrodynamically equivalent,[3] energy-scaled implosions[4–9] on OMEGA.[10]

These implosions are designed to achieve similar peak shell velocities (implosion velocity v_{imp}), hot-spot convergence (CR, ratio of initial inner-ice-surface radius and the hot-spot radius), in-flight aspect ratio [IFAR, defined as the ratio of the shell radius and the shell thickness (distance between the 1/*e* points with respect to the peak density) when the shell has reached 2/3 of its initial radius], as ignition designs.[2,3] Recent implosion experiments on OMEGA[9] reached record performance parameters, indicating that similar ignition-scale experiments would achieve a Lawson parameter $P\tau \sim 60\%$ of the value required for ignition,[11] where P is the pressure in the hot spot, and τ is the confinement time. This scaled $P\tau$ is similar to the values achieved in indirect-drive implosions at the National Ignition Facility (NIF).[12,13]

In these experiments, the inferred hot-spot pressure P is ~40% lower compared to one-dimensional (1-D) simulations,[9] indicating that the experimental performance is significantly degraded. The current hypothesis to explain this performance degradation for implosions with an adiabat >3.5 is based on low-mode hydrodynamic instabilities.[8,9,14] These hydro-instabilities can be seeded by long-wavelength nonuniformites in the initial conditions, like ice-thickness variations,[5] target offset,[5,15] and laser-drive nonuniformity in space and time (target placement, beam pointing, power balance, and beam timing). Isolated defects like the target stalk,[16] debris on the target surface, or short-wavelength structures like target-surface roughness[17] or laser imprint,[15,18] especially for low-adiabat implosions ($\alpha < 3.5$), can also seed these instabilities.

The performance of these experiments with layered cryogenic DT targets has been measured using nuclear and X-ray self-emission diagnostics.[8,9] Recent three-dimensional (3-D) hydro simulations[14] have indicated that the X-ray self-emission images show the influence of long-wavelength non-uniformities on the hot core and do not observe the assembly of the cold shell. Figure 1 shows an equatorial density map from 3-D *ASTER* simulations[14] (a) at peak neutron production compared to (b) a simulated self-emission image from an orthogonal polar view in the 4- to 8-keV X-ray band at the same time. The comparison between the density map and a simulated X-ray image demonstrates that the shape of the X-ray image does not follow the density distribution in the shell.

Note: Paper NI2 4, Bull. Am. Phys. Soc. **61**, 223 (2016).
[a)]Invited speaker.

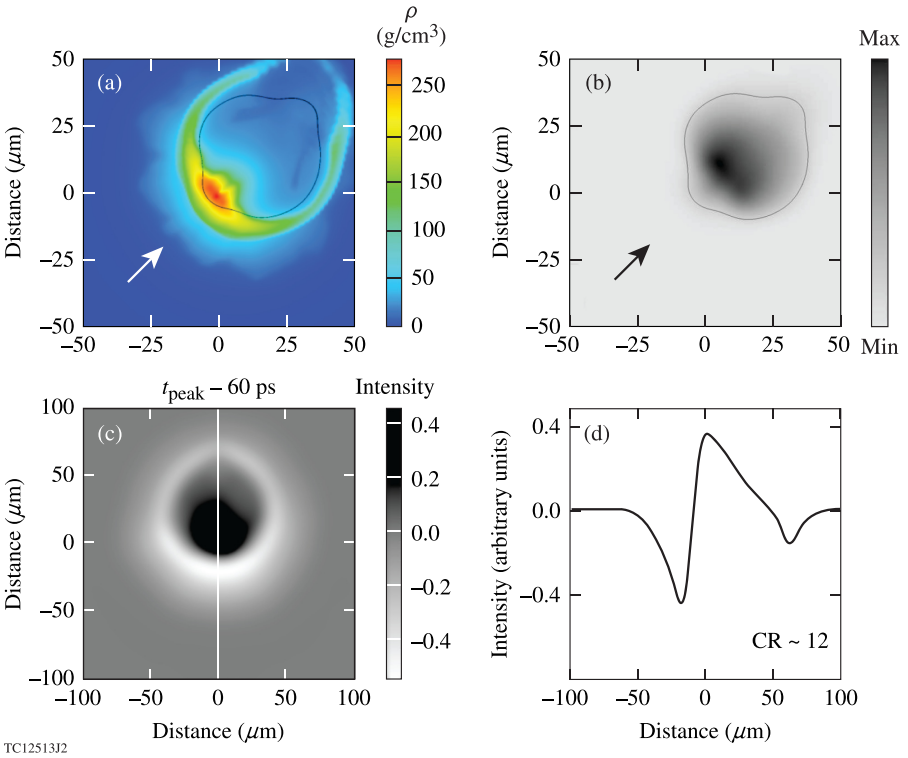

FIG. 1. (a) Equatorial distributions of the density from a 3-D radiation–hydrodynamic simulation at peak neutron production taken from Ref. 14. (b) Simulated self-emission image from a polar view in the 4- to 8-keV X-ray band at the same time. The direction of the 20-μm target offset is indicated by arrows. The thin black lines show the 17% contour of the maximum X-ray fluence in (b). (c) Simulated backlit image 50 ps before peak neutron production at a convergence ratio (CR) ~ 12. The image is oriented so that the vertical is along the target offset direction. (d) Vertical lineout through the backlit image.

X-ray backlighting can be used to observe the flow of the dense and relatively cold shell material in these cryo DT implosions. This technique has been used successfully in both direct-drive room-temperature experiments with gas-filled plastic (CH) targets[19] and in surrogate indirect-drive[20] ICF implosion experiments to measure the velocity and uniformity of the imploding shell. Figure 1(c) shows a simulated backlit image 50 ps before peak neutron production at a convergence ratio (CR) ~12. The image is oriented so that the vertical is along the target offset direction. The image shows the absorption of the dense shell as a white ring and the self-emission of the core, which is seen as a darker central feature. The dominant effect from the offset that will grow into a 5:1 density perturbation at peak compression is clearly visible in the image and measurable in the lineout [Fig. 1(d)] even at this relatively modest convergence.

Direct-drive cryogenic DT implosions on OMEGA are difficult to radiograph because of the low opacity of the DT shell, the high shell velocity, the small size of the stagnating shell, and the very bright self-emission of the hot core. A shaped crystal imaging system with a Si backlighter driven by short (10- to 20-ps) laser pulses from OMEGA EP,[21] was used to radiograph the OMEGA cryogenic implosions. It has the benefits of a narrow spectral width, high photon throughput, and a backlighter with a short emission time and high brightness. The main advantage of the monochromatic nature of this system is that it is possible to achieve similar brightness in the narrow spectral acceptance of the imager, which is matched to a resonance line of the backlighter, to the core of the implosion, which is a very broadband emitter, using much less energy in the laser driving the backlighter compared to the implosion driver. Processes with features below the spatial resolution of the imaging system like mix can be detected through the opacity effects from the carbon of the ablator material, which will significantly increase the absorption of the DT shell if mixing between the ablator and DT shell occurs.

This article is structured as follows: Sec. II presents the setup of the experiments, including a description of the narrowband crystal imaging system. Section III describes the experimental results in three subsections: (a) low-order modes, (b) stalk effects, and (c) mix. Section IV presents the conclusions.

II. EXPERIMENTAL SETUP

The cryogenic targets used in these experiments had an outer radius of ~430 to 480 μm. An ~8- to 12-μm-thick ablator shell of either plastic (CH), deuterated plastic (CD), or CD doped with 0.7% germanium encased a 50- to 75-μm-thick cryogenic DT ice layer [see Fig. 2(a)]. All targets were fully characterized using optical shadowgraphy and showed ice thickness variations of typically <1-μm root mean square (rms).[9] Triple-picket pulses of ~22- to 25-kJ laser energy were used to irradiate the targets, with smoothing by distributed phase plates (DPP's);[22] polarization smoothing (PS) with birefringent wedges;[23] two-dimensional (2-D), three-color-cycle, 0.33-THz smoothing by spectral dispersion (SSD);[24,25] optimized energy balance (<4% beam-to-beam);[26] and optimized beam-to-beam timing of ~10-ps rms (Ref. 14). The targets were placed within ~10 μm of the target chamber center.[14] The shape of the laser pulse was designed to put the shell on a specific adiabat that ranged from ~2 to 4 in these experiments. Figure 2(b) shows examples of both a lower- and a higher-adiabat pulse at comparable total laser energies. The high-adiabat pulses are shorter and have larger picket energies than the low-adiabat pulses. The total laser energy and the total shell mass determine the

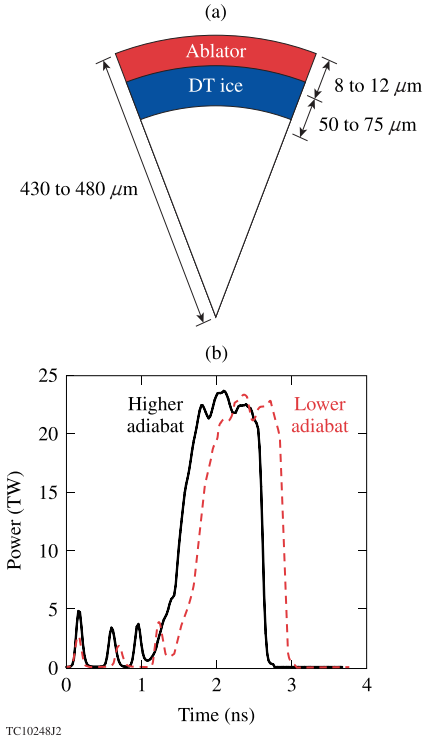

FIG. 2. (a) The cryogenic DT capsules consist of a thin, 8- to 12-μm CH, CD, or doped-CD ablator filled with several hundred atm of DT gas to create a 60- to 75-μm-thick ice layer at cryogenic temperatures below the triple point of DT ($\sim$19 K). (b) The laser drive pulse consists of a series of three pickets to establish the shell adiabat and control shock coalescence and a high-intensity main drive with a total energy of 22 to 25 kJ.

peak implosion velocity, which ranged from $v_{\mathrm{imp}} = 2.4$ to 3.7×10^7 cm/s. The IFAR ranged from 10 to 20 in these experiments. The IFAR is predominantly controlled by the shell thickness and shell adiabat.

A shaped Bragg crystal-imaging system was used to obtain radiographs of the imploding targets at various convergence ratios. The OMEGA crystal-imaging radiography system[21] (see Fig. 3) uses a Si backlighter driven by the OMEGA EP laser to backlight implosion targets driven by the 60 beams of the OMEGA laser (not shown for clarity). A quartz crystal, cut along the $10\underline{1}1$ planes for a $2d$ spacing of 0.6687 nm, was used for the Si He_α line at $\sim$1.865 keV (0.664 nm). The Bragg angle for this configuration was 83.9°. The crystal was mounted by direct optical contact on an aspheric glass substrate by INRAD.[27] The crystal has a major radius of curvature of 500 mm and is placed 267 mm from the implosion target. The image is recorded on a detector located $\sim$3.65 m

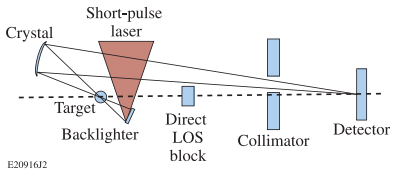

FIG. 3. Schematic of the spherical-crystal-imager backlighting setup from Ref. 21 (not to scale). The short-pulse laser illuminates a backlighter foil behind the primary target, which is heated by 60 beams from the OMEGA laser (not shown). A direct line-of-sight (LOS) block and a collimator protect the detector [an X-ray framing camera (XRFC)] from background X-rays emitted by the backlighter and primary targets.

from the target, for a magnification of $\sim$15×. The quartz crystal is rectangular with a size of 25 × 10 mm, resulting in an f number of $f = 10$ in the horizontal and $f = 25$ in the vertical direction. The spectral bandwidth of the imager is of the order of 10 eV, which matches the typical broadened linewidth of the resonance line from the backlighter driven by a short-pulse laser.

The available solid angle to place the backlighter foil is quite limited since the backlighter target must not intercept any of the 60 beams pointed at the implosion target. Because the backlighter laser intensity must be kept as high as possible, the 500-μm square backlighter was placed at a distance of 5 mm from the implosion target. Mounting the backlighter target on the same support structure as the cryogenic implosion target is not possible since it would distort the uniformity of the isotherms inside the layering sphere, which is essential for obtaining high-quality DT ice layers. A fast target insertion system (FASTPOS) inserts the backlighter target 100 ms after the shroud that protects the layered cryogenic target from ambient thermal radiation has been removed. FASTPOS also acts as the direct line-of-sight (LOS) block. Two additional collimators are placed on the mounting structure for the FASTPOS to suppress background from Compton scattering and fluorescence from structures in the target chamber. To reduce the impact of the self-emission of the hot core of the cryo DT implosion, an X-ray framing camera (XRFC) head[28] is used as a detector. The XRFC head is run with either a single-strip microchannel-plate (MCP) detector, with a 300 - to 500-ps-long exposure or a four-strip MCP with an exposure time of $\sim$40 ps, where the backlit image is placed in the center of one of the four strips. The spatial resolution of the XRFC recording system is typically $\sim$20 lp/mm (Ref. 29). Experiments with resolution grids show an $\sim$15-μm, 10% to 90% edge response for the crystal-imaging system. This spatial resolution is adequate for these initial experiments. Work is underway to improve the resolution to $<10\,\mu$m. The XRFC is triggered by an ultrastable electro-optical trigger system with a jitter of $\sim$1.5-ps rms. Experiments using only the backlighter foil showed that the XRFC system has a jitter of $<$10-ps rms with respect to the arrival of the OMEGA EP laser on the backlighter target. The timing of the OMEGA EP pulse to the OMEGA laser was measured to be $\sim$10-ps rms using the neutron temporal diagnostic (P11NTD),[30] which is also sensitive to the high-energy X-rays produced during the interaction of the OMEGA EP laser with the backlighter target.

Figure 4(a) shows the temporal evolution of the implosion from 1-D *LILAC*[31] simulations close to peak compression compared to the laser pulse shape (blue) for a typical backlit cryogenic implosion. All *LILAC* simulations shown in this paper include the effects of cross-beam energy transfer (CBET)[32] and use a nonlocal thermal-conduction model.[6] The trajectory of the shell radius (peak density: green; 1/e of peak density: black) starts at the $\sim$430-μm outer radius of the target and shows the shell moving toward the center until a peak compression at $\sim$3.5 ns. The neutron production rate (orange) peaks $\sim$40 ps before the calculated areal density (magenta). The exposure time of the XRFC is indicated in the gray-shaded area and the arrival time of the OMEGA EP short-pulse laser in red. A time-gated image of a backlit DT

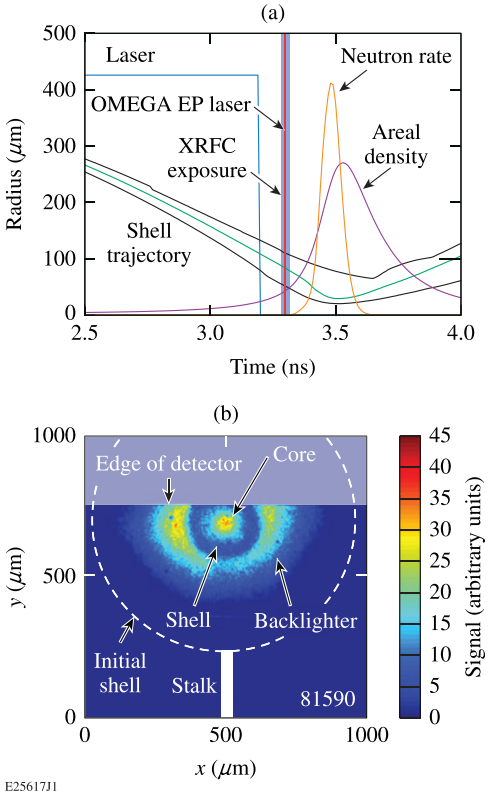

FIG. 4. (a) Trajectory of the shell radius (center: green; inner, outer edge: black) compared to the temporal history of the laser power (blue) and neutron production rate (orange) from 1-D *LILAC* simulations for the experiment shown in (b). The areal density evolution is shown for comparison (magenta). The exposure timing of the XRFC is indicated in the gray-shaded area and the arrival time of the OMEGA EP short-pulse laser in red. (b) Time-gated image of a backlit DT cryogenic implosion with an exposure time of ∼40 ps. The initial shell radius and the location of the stalk are shown for comparison.

cryogenic implosion with an exposure time of ∼40 ps is shown in Fig. 4(b). The dashed white line indicates the original shell diameter, and the white line at the bottom of the image shows the location of the target stalk. The backlighter emission is shown in the center of the image. It is clipped at the top of the XRFC slit because of a misalignment caused by repeatability issues in the crystal insertion mechanism. The absorption from the compressed shell is seen in the image as a ring-like feature around an emission feature from the central bright core of the implosion.

To measure the absorption in the compressed shell and to quantitatively compare the signal recorded by the crystal imager with simulations, the data must be corrected for the backlighter shape. A simple first-order physical model was constructed[21] to describe the shape of the backlighter by assuming a constant brightness source. This source was convolved with a Gaussian point-spread function (PSF), representing the spatial resolution of the imaging system at a 5-mm defocus. The brightness and extent of the source and the width of the PSF were varied to obtain a best fit to the shape of the measured signal outside the area affected by the absorption of the target. These uncertainties associated with correction are taken into account in the errors reported on the measured absorption.

III. EXPERIMENTAL RESULTS

A. Low-order modes

Long-wavelength nonuniformity can be seeded in an implosion by a number of processes including nonuniformities in the laser illumination, target placement, and thickness variations in both the ablator and the DT ice layer. To study the impact of these long-wavelength nonuniformities on the assembly of the compressed high-density shell close to stagnation, a series of experiments was performed with preimposed initial-thickness perturbations in the CH shell.

Figure 5 shows a sketch of a shaped target with preimposed initial thickness perturbations in the CH shell. The amplitude of the variation in shell thickness was 2 to 4 μm peak to peak. This variation caused an ∼1 to 2-μm amplitude variation in mode $\ell = 2$ of the inner radius of the ice layer during the layering process. The calculated ice thickness was still quite uniform and the mid-to high-mode ice roughness was not significantly different from a standard target. A fiducial glue spot of ∼30-μm diameter was used to orient the targets horizontally, i.e., perpendicular to the stalk that is mounted vertically in the target chamber. Standard-quality targets with an ablator thickness nonuniformity of <0.1-μm rms in all modes and a DT ice layer nonuniformity of <1.0-μm rms are used in separate experiments to establish a reference.

The radiograph from the reference experiment with a standard-quality target (shot 81590) from Fig. 4(b) is shown on an expanded scale in Fig. 6(a). The image is recorded at ∼100 ps before peak neutron production at a CR of 7, with an exposure time of ∼40 ps. The absorption of the backlighter from the compressed shell is seen in the image as a ringlike feature around a central emission feature from the bright core of the implosion. The initial CH ablator thickness of the target was ∼12 μm, with an outer diameter of ∼890 μm. The measured nonuniformity of the outer surface was 0.24-μm rms. The thickness of the DT ice layer was measured at ∼61 μm with a 0.5-μm–rms thickness variation. The

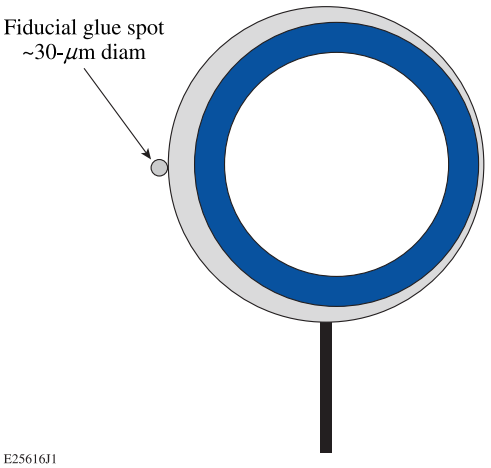

FIG. 5. Illustration of a shaped target with a horizontal variation in the CH shell thickness. The amplitude of this variation was 2- to 4-μm peak to peak. This variation caused an ∼1- to 2-μm amplitude variation in the inner radius of the ice layer. A fiducial glue spot of ∼30-μm diameter was used to orient the targets with respect to the stalk.

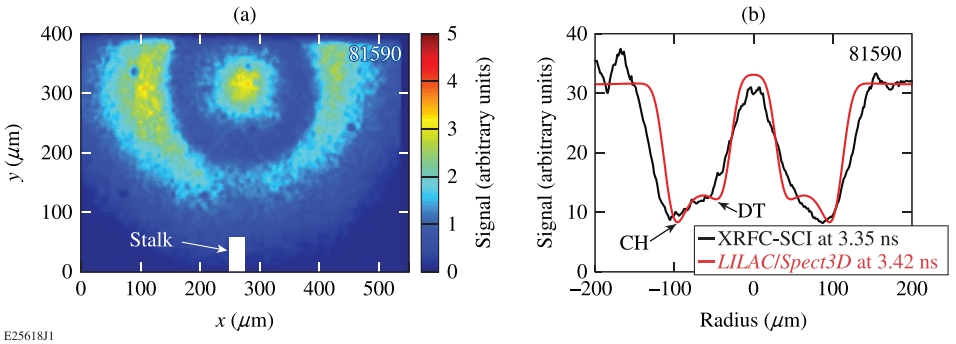

FIG. 6. (a) Backlit image of cryogenic implosion (shot 81590). (b) Backlighter shape corrected horizontal lineout compared to *Spect3D* post-processed, 1-D *LILAC* simulations.

target was imploded with a triple picket pulse of 24-kJ energy at a calculated adiabat of ∼2.5, which led to a calculated IFAR = 10. The measured offset from target chamber center at shot time was <10 μm. The recorded yield was 20% of the 1-D calculations (yield over clean: YOC) and the measured areal density was ∼80% of the predictions.

Figure 6(b) shows the backlighter shape corrected horizontal lineout of the radiograph in Fig. 6(a) compared to *Spect3D*[33] post-processed, 1-D *LILAC* simulations. The backlighter intensity was adjusted to match the observed ratio of backlighter relative to the level of self-emission of the core. The measured spatial resolution of the imager of ∼15 μm was taken into account in the *Spect3D* post-processing. The simulated lineout matches the experiment quite closely in both size and magnitude of the absorption. The most-noticeable difference between experiment and simulation is that the slopes of the signal at the interface between shell and core and at the outside of the shell are significantly steeper in the simulation.

To further analyze the radiographs and to obtain quantitative data on the shape of the compressed shell, radial lineouts were taken from the center of the self-emission peak, and the radius of peak absorption and its magnitude were evaluated as a function of azimuthal angle (see Fig. 7). The contour at 1/*e* of the peak of the core emission is also determined and plotted in Fig. 7(a) for comparison. The errors shown in the graph are estimates of the uncertainty determining the peak absorption location or the 1/*e* of the emission given the signal/noise on the experimental signal. The radius of peak absorption shows predominantly a $\ell = 1$–like feature of ∼10-μm amplitude, with a small extra feature at 180° azimuthal angle, which is associated with the stalk (see Sec. III B). Within the errors of the evaluation, the 1/*e* contour of the core self-emission is observed to be circular. The magnitude of peak absorption shows a small ∼±5% peak-to-peak variation as a function of the angle.

A radiograph obtained in an experiment using a shaped target with a 4-μm peak-to-peak variation in the CH ablator wall thickness (shot 82717) is shown in Fig. 8(a). The image was recorded at a CR = 10, ∼50 ps before peak neutron production. The gate time of the XRFC was ∼40 ps. Because of drifts in the OMEGA EP beam pointing, the registration between the backlighter emission and the implosion is not as good as it was for shot 81590. Nevertheless, the absorption feature from the compressed shell is clearly visible. Since the image was recorded ∼50 ps closer to peak neutron production and at peak X-ray emission, the emission of the central core is brighter than in the shot shown in Fig. 6. The target had an outer diameter of ∼960 μm, with an initial CH ablator thickness of ∼11 μm. The measured total variation in the inner DT ice layer radius was ∼2-μm rms, and its thickness was ∼63 μm. The nonuniformity of the outer surface radius was 0.21-μm rms. The target was irradiated with a triple-picket pulse of 25-kJ energy at a calculated adiabat of ∼2.0. The calculated IFAR was 14. The measured offset from target chamber center at shot time was <10 μm. The observed YOC was 8%, and the measured areal density was ∼40% of the calculated value.

Figure 8(b) shows the backlighter shape-corrected horizontal lineout of the radiograph in Fig. 8(a) compared to *Spect3D* post-processed, 1-D *LILAC* simulations, where the backlighter intensity was adjusted to match the observed self-emission of the core. The simulated lineout does not match the experiment quite as well as it did for the comparison shot 81590. While the shape of the self-emission peak is reproduced quite well, the absorption feature from the compressed shell is significantly underestimated. The experimental lineout

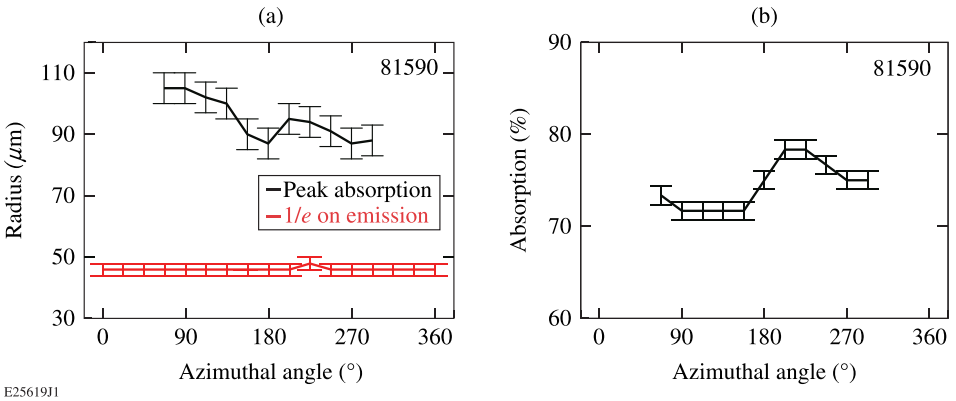

FIG. 7. (a) Radius of peak absorption as a function of angle obtained by evaluating lineouts taken from the center of the self-emission peak (shot 81590). The 1/*e* radius contour from the self-emission is shown for comparison. (b) Peak absorption as a function of angle.

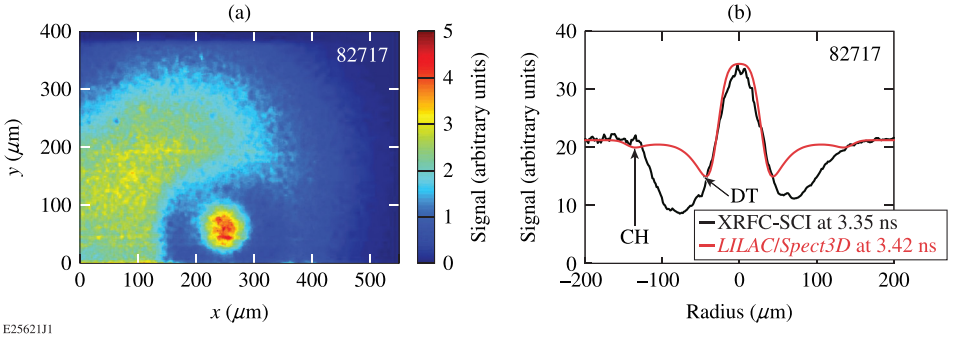

FIG. 8. (a) Backlit image of cryogenic implosion shot 82717 using a shaped target with a 4-μm variation in peak-to-peak CH shell thickness. (b) Backlighter shape-corrected horizontal line out compared to *Spect3D* post-processed 1-D *LILAC* simulations.

shows a significant left–right asymmetry, which is consistent with the initial placement of the target, where the thicker side of the CH ablator is placed on the left side of the image shown in Fig. 8(a).

The radius of peak absorption and its magnitude are evaluated again as a function of azimuthal angle, together with the contour at $1/e$ of the peak of the core emission, (see Fig. 9). The radius of peak absorption shows a feature of $\sim$20-μm amplitude. Clipping on the XRFC strip caused by the pointing instability of the crystal-insertion mechanism made it impossible to extract data in the stalk region around the 180° azimuthal angle. The $1/e$ contour of the core self-emission shows a measurable $\ell = 2$–type variation with an amplitude of $\sim$7 μm. A much larger perturbation in the magnitude of peak absorption as a function of an angle of $\sim\pm$20% is observed with the shaped shell compared to the reference shell. The removal of the backlighter profile, which has a strong left–right asymmetry for the data shown in Fig. 8(b), adds additional error in the determination of the absorption, especially on the right side of the image (180° to 360°), because of the larger gradient on the backlighter intensity on the right side compared to the left side. Consequently the error bars shown in Fig. 8(b), are twice as large on the right side compared to the left side. The determination of the radius of peak absorption is not significantly affected by the removal of the backlighter shape since the gradients at this radius are still small; the errors are dominated by the photon statistics noise.

The backlit images show that even for the reference implosion without any preimposed nonuniformity, deviations from a spherical shell assembly can be seen. Additionally, the fact that the interfaces between shell and core and at the outside of the shell are significantly steeper in the simulation indicates that there is probably a small-scale mixing occurring in the deceleration phase that cannot be spatially resolved with the imager and therefore is visible only in the change of the gradients compared to 1-D simulations. The radiograph for the reference implosion also shows that the shape of the dense shell where a significant $\ell = 1$ perturbation is visible, does not necessarily correspond to the shape of the hot spot, which is seen to be round.

The images from the experiments using targets with preimposed CH ablator thickness variations show much larger perturbations than the reference implosion, both in the radius and magnitude of peak absorptions. The lineouts show significantly more absorption over a larger radius than the post-processed 1-D simulation, indicating more mixing between the ablator CH and the DT ice layer. Even though the targets and laser pulses are quite similar, the small differences in adiabat in the IFAR lead to significant differences in the shape of the absorption features as compared to simulations.

B. Stalk effects

The impact of the target stalk and the glue spot, with which the stalk is attached to the shell, on the implosion symmetry has been observed previously using the crystal-imaging system in an implosion experiment with a mass equivalent CH target fielded from the cryo target insertion system.[21] At a convergence of 2.5, the image revealed a cusp-like feature in the shell radius at the location of the stalk. Figure 10(a) shows the shell radius as a function of azimuthal angle, evaluated at 50% point on the absorption feature seen in the backlit image of the mass equivalent CH target (shot 69789). The target had a shell thickness of 24 μm and was irradiated with 23 kJ of laser energy. The evaluation shows a narrow feature of $\sim$25-μm amplitude at the

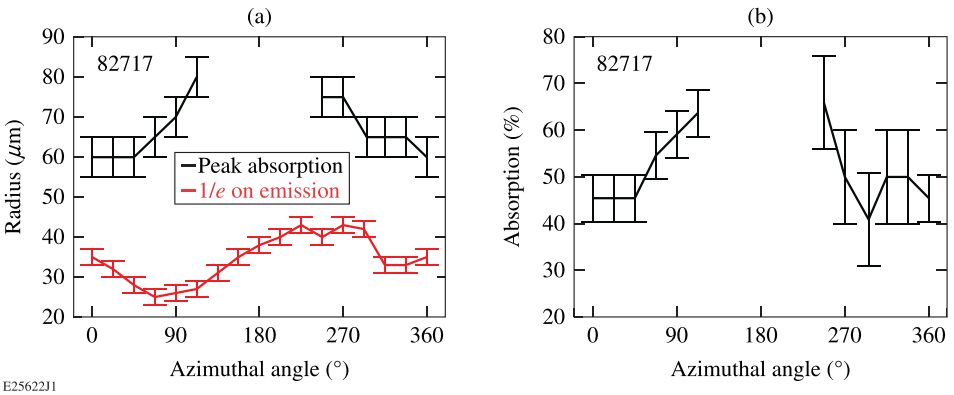

FIG. 9. (a) Radius of peak absorption as a function of angle obtained by evaluating lineouts taken from the center of the self-emission peak (shot 82717). The $1/e$ radius contour from the self-emission is shown for comparison. (b) Peak absorption as a function of angle.

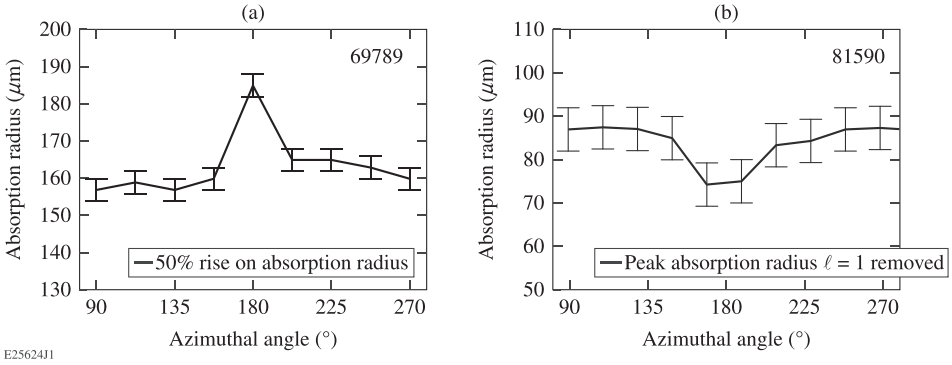

FIG. 10. (a) Shell radius as a function of angle, inferred from the 50% point on the absorption feature seen in the backlit image of a mass equivalent CH target as shown in Ref. 20 (shot 69789). (b) Radius of peak absorption as a function of angle, obtained by taking lineouts from the center of the image from the cryo implosion shown in Fig. 5 (shot 81590). An $\ell = 1$ mode of 10-μm amplitude was removed to show the effect of the stalk more clearly.

stalk location at 180° azimuthal angle. At the stalk feature, the shell radius is larger than the average shell radius.

Figure 10(b) shows the radius of peak absorption as a function of angle at a convergence of 7, obtained by taking lineouts from the center of the image from cryo implosion shown in Fig. 5 (shot 81590). An $\ell = 1$ mode of 10-μm amplitude was removed to show the effect of the stalk more clearly. The radius of peak absorption shows a relatively wide feature of ∼45° extend in azimuthal angle and an amplitude of ∼10 μm. In this case, the shell radius is smaller at the stalk feature than the average shell radius.

The change in direction of the stalk perturbation from being larger than the average radius at CR = 2.5 during the acceleration phase to being smaller than the average radius at CR = 7 during the deceleration phase is expected based on an analysis of multidimensional hydro simulations. During acceleration, the stalk area lags behind the rest of the shell because the extra mass of the glue and the shadowing of the laser drive by the stalk reduce the shell velocity. During deceleration, the extra mass at the stalk location causes it to decelerate more slowly against the growing pressure of the core, allowing it to push farther in compared to the average shell.

C. Imprint and mix

The images from most cryogenic DT target experiments show significantly more contrast than expected from *Spect3D* post-processed *LILAC* simulations, which indicates that carbon from the ablator mixes into the DT ice layer.

Figure 11 shows a lineout through the image of shot 70535 corrected for the backlighter shape. A 300-ps gate was used in these experiments and was timed to start ∼500 ps before the calculated time of peak core emission, according to 1-D *LILAC* hydrocode simulations. The OMEGA EP short-pulse laser was fired ∼100 ps before the end of the gate at a time when the shell assembly was compressed to an inner radius of ∼90 μm, which translates to a convergence of ∼4, given an inner ice shell radius of ∼380 μm. The calculated areal density of the DT at this convergence was ∼14 mg/cm^2 with an adiabat of 2.5. The simulations show an IFAR = 12 for this implosion.

The result from a 1-D *LILAC* simulation, post-processed with the radiation transport code *Spect3D*, is plotted for comparison on the left side of the experimental lineout (green line). The backlighter timing had to be shifted ∼50 ps earlier to match the measured size of the absorption feature, indicating that the implosion was slightly delayed compared to the simulations. The timing of the OMEGA EP laser during these experiments was not as well controlled as it was for the shots with the 40-ps-exposure-time framing camera and had a jitter of the order of 20-ps rms. The long exposure and the large trigger jitter make it very difficult to obtain a reliable and accurate match with simulations of the self-emission contribution, so the simulation data are shown without the contribution from self-emission. The measured absorption was much higher than the absorption calculated from the simulations. One possible explanation for this discrepancy is Rayleigh–Taylor mixing of carbon from the outer CD shell into the DT ice during the shell acceleration. Adding a small amount of carbon uniformly into the shell in the *Spect3D* post-processor [0.1% C (blue line), 0.2% C (red line)] significantly increases the absorption in the model and brings the simulation much closer to the experimental data, especially in the areas of highest absorption corresponding to the dense shell. In the center of the image, the calculated absorption with carbon mixing is higher than observed. This is probably caused by a small amount of self-emission, which is not fully suppressed by the gating.

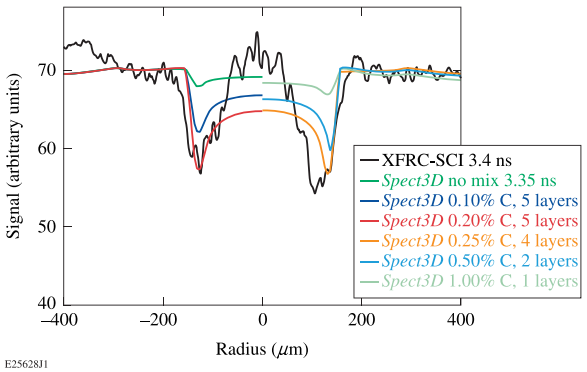

FIG. 11. Backlighter shape–corrected lineout through the radiograph of a cryogenic target shown in Ref. 21 (black line) compared to a *Spect3D* post-processed *LILAC* simulation (colored lines). In the simulation, the DT ice was split into five layers, and the CH was mixed into these layers uniformly. The left side of the image shows that simulations with a uniform mix of 0.2% C into the DT match the experimental data (green, blue, and red lines). The right side of the image shows results from simulations where the same mass of C is added to the DT, penetrating into more and more layers (light green, cyan, orange), showing that at least four layers need to be mixed for and adequately matched to the experimental data.

To estimate the depth of the mixing of carbon into the DT, the DT shell was split into five regions of equal thickness in the 1-D *LILAC* simulations. An equivalent mass of 0.2% C (atomic) was mixed either into the full DT shell or in the outer one, two, or four layers in the *Spect3D* post-processor. The results from *Spect3D* are shown on the right side of Fig. 11. The one-layer simulations (light green) show almost the same absorption as the unmixed simulations, indicating that the outermost 20% of the DT ice has already ablated at the time the radiograph was recorded, consistent with the predictions from the 1-D *LILAC* simulations. The two-layer simulation (cyan) shows significantly more absorption but still does not match the experiment. Even the four-layer absorption does not compare as well to the experiment as the fully mixed data, indicating that the carbon is most probably fully mixed throughout the DT shell.

Figure 12 shows the backlighter shape–corrected lineouts through the radiographs from two additional cryogenic target experiments compared to *Spect3D* post-processed *LILAC* simulations. The lineouts show only one side of the implosion because they could not be corrected for the backlighter shape due to a significant misalignment of the backlighter. The target in shot 80543 had a 8-μm CD shell doped with 0.7% germanium (atomic) and a 50-μm-thick DT ice layer. It was imploded with 25 kJ of laser energy using a pulse that set the calculated adiabat of the shell to ~2. Preheat from the Ge dopant caused the adiabat to rise to 3.5 at the end of the laser pulse. The IFAR of the shell was calculated to be 20. The radiograph was taken with a 40-ps-wide gate, ~150 ps before peak neutron production at a CR = 5 and a predicted areal density of ~40 mg/cm^2. Shot 75372 used a target with a 7-μm pure CD shell without any dopant and a 75-μm-thick DT ice layer. It was imploded with a 23 kJ of laser energy with a calculated adiabat of the shell of 4. The calculated IFAR was 20. The radiograph was recorded with a 200-ps XRFC gate, 150 ps before bang time at a CR = 7, and a predicted areal density of ~40 mg/cm^2.

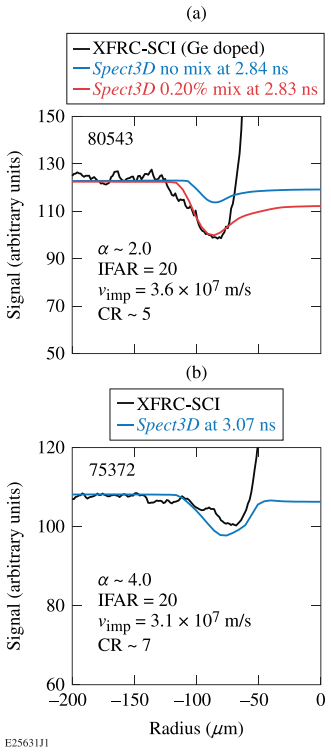

FIG. 12. Backlighter shape–corrected lineouts through the radiographs from two cryogenic target experiments compared to *Spect3D* post-processed *LILAC* simulations. Mixing of ablator material is required to match the experimental data for a Ge-doped low-adiabat ($\alpha = 2.5$) shot (80543) but not for a high-adiabat ($\alpha = 4.0$) implosion (75372).

Mixing of the ablator material at a level of ~0.2% is required to match the experimental data for the low-adiabat, Ge-doped shot (80543), similar to the mix observed in the low-adiabat, pure-CD shot (70535). No indication of mixing is observed in the higher-adiabat implosion (75372). In both radiographs, strong self-emission from the core is observed.

The radiography data show that the most important parameter controlling the mix from the CH/CD outer shell into the ice seems to be the adiabat since even a stable, very low IFAR = 10 implosion (70535) shows a significant mix throughout the DT quite early on in the implosion at the end of the acceleration phase, well before the deceleration of the shell has started. Two similar IFAR = 20 implosions show a mix threshold in adiabat at around $\alpha = 4$. The magnitude of the mixing appears to be quite small (~0.2%), which is most likely due to the fact that the DT is starting to be ablated quite early in the implosion. The analysis using five layers for shot 70535 shows that at least the outer 20% of the DT shell gets ablated before the end of the acceleration phase. This ablated DT could serve as a buffer between the CD and the dense DT shell that limits the mix.

IV. CONCLUSIONS

X-ray backlighting has been used to radiograph the compressed shell in implosion experiments with layered cryogenic DT targets on OMEGA at convergence ratios from 4 to 10. A shaped crystal imaging system with a Si backlighter driven by short laser pulses from OMEGA EP has been set up for this challenging radiography configuration.

The effects of long-wavelength nonuniformities on the shell assembly close to stagnation have been studied in an experiment with preimposed initial thickness perturbations in the CH shell. The radiograph from the reference implosion without any preimposed modulations shows a significant $\ell = 1$ perturbation in the shape of the dense shell, which does not match the shape of the hot spot. Additionally, indications of small-scale mixing are observed at the interfaces between ablator, DT shell, and the hot core. The images from targets with preimposed thickness variations show much larger perturbations than the reference implosion, in both the radius and magnitude of peak absorptions and significantly more mixing between the ablator CH and the DT ice layer.

The impact of the target stalk and the glue spot—with which the shell is attached to the stalk—on the implosion symmetry has been observed in both mass-equivalent CH targets and layered DT cryo targets. As expected from simulations, the stalk area lags behind the rest of the shell in the acceleration phase because the extra mass of the glue and the shadow from the stalk reduce the shell velocity and push in

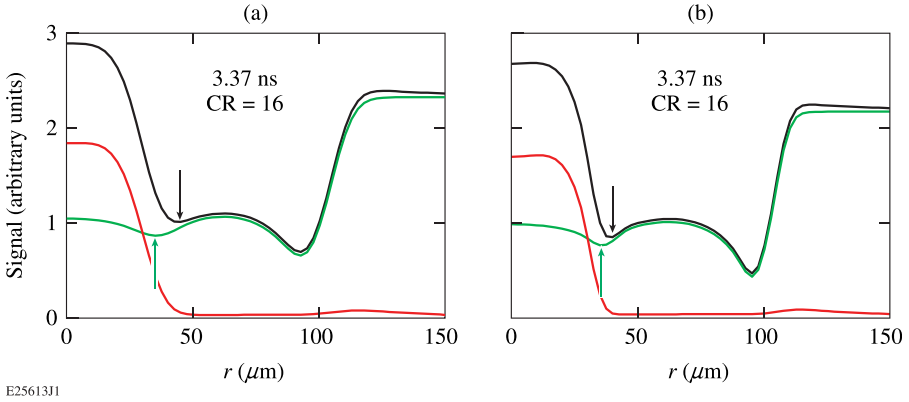

FIG. 13. Radial lineouts from *Spect3D* post-processed *LILAC* simulation of cryogenic implosions at a convergence ratio of 16 using (a) the measured spatial resolution of ∼15 μm and (b) an improved resolution of 8 μm. The green lines show the absorption of the DT and CH shell, the red line shows the self-emission from the core, and the black line shows the combination of both effects. The top black arrows indicate the location of the minimum absorption feature from the DT shell with self-emission and the bottom green arrows indicate the minimum absorption without self-emission.

farther during the deceleration phase because of the extra mass at the stalk location.

The experimental data show that the most important parameter controlling the mix from the CH/CD outer shell into the ice is the adiabat. A threshold in adiabat at around $\alpha = 4$ has been observed, where mix is below the detection threshold of 0.02%. The magnitude of the mixing appears to be quite small at ∼0.2%, which is most likely caused by the fact that the DT is starting to be ablated quite early in the implosion, thereby serving as a buffer between the CD and the dense DT shell, which could limit the amount of mix.

Future experiments will use this radiography technique to separate the performance degradation from different sources of nonuniformity like target offset compared to laser energy imbalance and to compare with detailed multidimensional hydrocode calculations. A project has been started that will improve the spatial resolution of the shaped crystal imager and increase the brightness of the backlighter in order to radiograph the implosions at a higher convergence closer to peak neutron production. To illustrate the benefit from a higher spatial resolution radial lineouts from *Spect3D* post-processed *LILAC* simulation of cryogenic implosions at a convergence ratio of CR = 16 are shown in Fig. 13. using either (a) the measured spatial resolution of ∼15 μm or (b) an improved resolution of 8 μm. The green lines show the absorption of the DT and CH shell, the red line shows the self-emission from the core, and the black line shows the combination of both effects. With the lower resolution of ∼15 μm, the location of the minimum absorption feature from the DT shell with self-emission, indicated by the top black arrow, is seen at a significantly different radius than the minimum absorption without self-emission, indicated by the bottom green arrow. This discrepancy is reduced at the higher resolution of 8 μm, which will allow a more-accurate determination of the location of the dense DT in the presence of self-emission.

ACKNOWLEDGMENTS

This material is based upon work supported by the Department of Energy National Nuclear Security Administration under Award No. DE-NA0001944, the University of Rochester, and the New York State Energy Research and Development Authority. The support of DOE does not constitute an endorsement by DOE of the views expressed in this article.

This report was prepared as an account of work sponsored by an agency of the U.S. Government. Neither the U.S. Government nor any agency thereof, nor any of their employees, makes any warranty, express or implied, or assumes any legal liability or responsibility for the accuracy, completeness, or usefulness of any information, apparatus, product, or process disclosed, or represents that its use would not infringe the privately owned rights. Reference herein to any specific commercial product, process, or service by trade name, trademark, manufacturer, or otherwise does not necessarily constitute or imply its endorsement, recommendation, or favoring by the U.S. Government or any agency thereof. The views and opinions of authors expressed herein do not necessarily state or reflect those of the U.S. Government or any agency thereof.

[1]R. S. Craxton, K. S. Anderson, T. R. Boehly, V. N. Goncharov, D. R. Harding, J. P. Knauer, R. L. McCrory, P. W. McKenty, D. D. Meyerhofer, J. F. Myatt, A. J. Schmitt, J. D. Sethian, R. W. Short, S. Skupsky, W. Theobald, W. L. Kruer, K. Tanaka, R. Betti, T. J. B. Collins, J. A. Delettrez, S. X. Hu, J. A. Marozas, A. V. Maximov, D. T. Michel, P. B. Radha, S. P. Regan, T. C. Sangster, W. Seka, A. A. Solodov, J. M. Soures, C. Stoeckl, and J. D. Zuegel, Phys. Plasmas **22**, 110501 (2015).

[2]V. N. Goncharov, S. P. Regan, E. M. Campbell, T. C. Sangster, P. B. Radha, J. F. Myatt, D. H. Froula, R. Betti, T. R. Boehly, J. A. Delettrez, D. H. Edgell, R. Epstein, C. J. Forrest, V. Yu. Glebov, D. R. Harding, S. X. Hu, I. V. Igumenshchev, F. J. Marshall, R. L. McCrory, D. T. Michel, W. Seka, A. Shvydky, C. Stoeckl, W. Theobald, and M. Gatu-Johnson, Plasma Phys. Controlled Fusion **59**, 014008 (2017).

[3]V. N. Goncharov, T. C. Sangster, R. Betti, T. R. Boehly, M. J. Bonino, T. J. B. Collins, R. S. Craxton, J. A. Delettrez, D. H. Edgell, R. Epstein, R. K. Follet, C. J. Forrest, D. H. Froula, V. Yu. Glebov, D. R. Harding, R. J. Henchen, S. X. Hu, I. V. Igumenshchev, R. Janezic, J. H. Kelly, T. J. Kessler, T. Z. Kosc, S. J. Loucks, J. A. Marozas, F. J. Marshall, A. V. Maximov, R. L. McCrory, P. W. McKenty, D. D. Meyerhofer, D. T. Michel, J. F. Myatt, R. Nora, P. B. Radha, S. P. Regan, W. Seka, W. T. Shmayda, R. W. Short, A. Shvydky, S. Skupsky, C. Stoeckl, B. Yaakobi, J. A. Frenje, M. Gatu-Johnson, R. D. Petrasso, and D. T. Casey, Phys. Plasmas **21**, 056315 (2014).

[4]C. Stoeckl, C. Chiritescu, J. A. Delettrez, R. Epstein, V. Yu. Glebov, D. R. Harding, R. L. Keck, S. J. Loucks, L. D. Lund, R. L. McCrory, P. W. McKenty, F. J. Marshall, D. D. Meyerhofer, S. F. B. Morse, S. P. Regan, P. B. Radha, S. Roberts, T. C. Sangster, W. Seka, S. Skupsky, V. A.

Smalyuk, C. Sorce, J. M. Soures, R. P. J. Town, J. A. Frenje, C. K. Li, R. D. Petrasso, F. H. Séguin, K. Fletcher, S. Padalino, C. Freeman, N. Izumi, R. Lerche, and T. W. Phillips, Phys. Plasmas **9**, 2195 (2002).
[5]F. J. Marshall, R. S. Craxton, J. A. Delettrez, D. H. Edgell, L. M. Elasky, R. Epstein, V. Yu. Glebov, V. N. Goncharov, D. R. Harding, R. Janezic, R. L. Keck, J. D. Kilkenny, J. P. Knauer, S. J. Loucks, L. D. Lund, R. L. McCrory, P. W. McKenty, D. D. Meyerhofer, P. B. Radha, S. P. Regan, T. C. Sangster, W. Seka, V. A. Smalyuk, J. M. Soures, C. Stoeckl, S. Skupsky, J. A. Frenje, C. K. Li, R. D. Petrasso, and F. H. Séguin, Phys. Plasmas **12**, 056302 (2005).
[6]V. N. Goncharov, T. C. Sangster, P. B. Radha, R. Betti, T. R. Boehly, T. J. B. Collins, R. S. Craxton, J. A. Delettrez, R. Epstein, V. Yu. Glebov, S. X. Hu, I. V. Igumenshchev, J. P. Knauer, S. J. Loucks, J. A. Marozas, F. J. Marshall, R. L. McCrory, P. W. McKenty, D. D. Meyerhofer, S. P. Regan, W. Seka, S. Skupsky, V. A. Smalyuk, J. M. Soures, C. Stoeckl, D. Shvarts, J. A. Frenje, R. D. Petrasso, C. K. Li, F. Séguin, W. Manheimer, and D. G. Colombant, Phys. Plasmas **15**, 056310 (2008).
[7]T. C. Sangster, V. N. Goncharov, R. Betti, T. R. Boehly, D. T. Casey, T. J. B. Collins, R. S. Craxton, J. A. Delettrez, D. H. Edgell, R. Epstein, K. A. Fletcher, J. A. Frenje, V. Yu. Glebov, D. R. Harding, S. X. Hu, I. V. Igumenshchev, J. P. Knauer, S. J. Loucks, C. K. Li, J. A. Marozas, F. J. Marshall, R. L. McCrory, P. W. McKenty, D. D. Meyerhofer, P. M. Nilson, S. P. Padalino, R. D. Petrasso, P. B. Radha, S. P. Regan, F. H. Seguin, W. Seka, R. W. Short, D. Shvarts, S. Skupsky, V. A. Smalyuk, J. M. Soures, C. Stoeckl, W. Theobald, and B. Yaakobi, Phys. Plasmas **17**, 056312 (2010).
[8]T. C. Sangster, V. N. Goncharov, R. Betti, P. B. Radha, T. R. Boehly, D. T. Casey, T. J. B. Collins, R. S. Craxton, J. A. Delettrez, D. H. Edgell, R. Epstein, C. J. Forrest, J. A. Frenje, D. H. Froula, M. Gatu-Johnson, V. Yu. Glebov, D. R. Harding, M. Hohenberger, S. X. Hu, I. V. Igumenshchev, R. Janezic, J. H. Kelly, T. J. Kessler, C. Kingsley, T. Z. Kosc, J. P. Knauer, S. J. Loucks, J. A. Marozas, F. J. Marshall, A. V. Maximov, R. L. McCrory, P. W. McKenty, D. D. Meyerhofer, D. T. Michel, J. F. Myatt, R. D. Petrasso, S. P. Regan, W. Seka, W. T. Shmayda, R. W. Short, A. Shvydky, S. Skupsky, J. M. Soures, C. Stoeckl, W. Theobald, V. Versteeg, B. Yaakobi, and J. D. Zuegel, Phys. Plasmas **20**, 056317 (2013).
[9]S. P. Regan, V. N. Goncharov, I. V. Igumenshchev, T. C. Sangster, R. Betti, A. Bose, T. R. Boehly, M. J. Bonino, E. M. Campbell, D. Cao, T. J. B. Collins, R. S. Craxton, A. K. Davis, J. A. Delettrez, D. H. Edgell, R. Epstein, C. J. Forrest, J. A. Frenje, D. H. Froula, M. Gatu Johnson, V. Yu. Glebov, D. R. Harding, M. Hohenberger, S. X. Hu, D. Jacobs-Perkins, R. T. Janezic, M. Karasik, R. L. Keck, J. H. Kelly, T. J. Kessler, J. P. Knauer, T. Z. Kosc, S. J. Loucks, J. A. Marozas, F. J. Marshall, R. L. McCrory, P. W. McKenty, D. D. Meyerhofer, D. T. Michel, J. F. Myatt, S. P. Obenschain, R. D. Petrasso, R. B. Radha, B. Rice, M. Rosenberg, A. J. Schmitt, M. J. Schmitt, W. Seka, W. T. Shmayda, M. J. Shoup III, A. Shvydky, S. Skupsky, S. Solodov, C. Stoeckl, W. Theobald, J. Ulreich, M. D. Wittman, K. M. Woo, B. Yaakobi, and J. D. Zuegel, Phys. Rev. Lett. **117**, 025001 (2016).
[10]T. R. Boehly, D. L. Brown, R. S. Craxton, R. L. Keck, J. P. Knauer, J. H. Kelly, T. J. Kessler, S. A. Kumpan, S. J. Loucks, S. A. Letzring, F. J. Marshall, R. L. McCrory, S. F. B. Morse, W. Seka, J. M. Soures, and C. P. Verdon, Opt. Commun. **133**, 495 (1997).
[11]A. Bose, K. M. Woo, R. Betti, E. M. Campbell, D. Mangino, A. R. Christopherson, R. L. McCrory, R. Nora, S. P. Regan, V. N. Goncharov, T. C. Sangster, C. J. Forrest, J. Frenje, M. Gatu Johnson, V. Yu. Glebov, J. P. Knauer, F. J. Marshall, C. Stoeckl, and W. Theobald, Phys. Rev. E **94**, 011201(R) (2016).
[12]O. A. Hurricane, D. A. Callahan, D. T. Casey, P. M. Celliers, C. Cerjan, E. L. Dewald, T. R. Dittrich, T. Döppner, D. E. Hinkel, L. F. Berzak Hopkins, J. L. Kline, S. Le Pape, T. Ma, A. G. MacPhee, J. L. Milovich, A. Pak, H.-S. Park, P. K. Patel, B. A. Remington, J. D. Salmonson, P. T. Springer, and R. Tommasini, Nature **506**, 343 (2014).
[13]R. Betti, A. R. Christopherson, B. K. Spears, R. Nora, A. Bose, J. Howard, K. M. Woo, M. J. Edwards, and J. Sanz, Phys. Rev. Lett. **114**, 255003 (2015).
[14]I. V. Igumenshchev, V. N. Goncharov, F. J. Marshall, J. P. Knauer, E. M. Campbell, C. J. Forrest, D. H. Froula, V. Yu. Glebov, R. L. McCrory, S. P. Regan, T. C. Sangster, S. Skupsky, and C. Stoeckl, Phys. Plasmas **23**, 052702 (2016).
[15]S. X. Hu, V. N. Goncharov, P. B. Radha, J. A. Marozas, S. Skupsky, T. R. Boehly, T. C. Sangster, D. D. Meyerhofer, and R. L. McCrory, Phys. Plasmas **17**, 102706 (2010).
[16]I. V. Igumenshchev, F. J. Marshall, J. A. Marozas, V. A. Smalyuk, R. Epstein, V. N. Goncharov, T. J. B. Collins, T. C. Sangster, and S. Skupsky, Phys. Plasmas **16**, 082701 (2009).
[17]I. V. Igumenshchev, V. N. Goncharov, W. T. Shmayda, D. R. Harding, T. C. Sangster, and D. D. Meyerhofer, Phys. Plasmas **20**, 082703 (2013).
[18]S. X. Hu, D. T. Michel, A. K. Davis, R. Betti, P. B. Radha, E. M. Campbell, D. H. Froula, and C. Stoeckl, Phys. Plasmas **23**, 102701 (2016).
[19]P. B. Radha, F. J. Marshall, J. A. Marozas, A. Shvydky, I. Gabalski, T. R. Boehly, T. J. B. Collins, R. S. Craxton, D. H. Edgell, R. Epstein, J. A. Frenje, D. H. Froula, V. N. Goncharov, M. Hohenberger, R. L. McCrory, P. W. McKenty, D. D. Meyerhofer, R. D. Petrasso, T. C. Sangster, and S. Skupsky, Phys. Plasmas **20**, 056306 (2013).
[20]D. G. Hicks, B. K. Spears, D. G. Braun, R. E. Olson, C. M. Sorce, P. M. Celliers, G. W. Collins, and O. L. Landen, Phys. Plasmas **17**, 102703 (2010).
[21]C. Stoeckl, M. Bedzyk, G. Brent, R. Epstein, G. Fiksel, D. Guy, V. N. Goncharov, S. X. Hu, S. Ingraham, D. W. Jacobs-Perkins, R. K. Jungquist, F. J. Marshall, C. Mileham, P. M. Nilson, T. C. Sangster, M. J. Shoup III, and W. Theobald, Rev. Sci. Instrum. **85**, 11E501 (2014).
[22]Y. Lin, T. J. Kessler, and G. N. Lawrence, Opt. Lett. **20**, 764 (1995).
[23]T. R. Boehly, V. A. Smalyuk, D. D. Meyerhofer, J. P. Knauer, D. K. Bradley, R. S. Craxton, M. J. Guardalben, S. Skupsky, and T. J. Kessler, J. Appl. Phys. **85**, 3444 (1999).
[24]S. Skupsky, R. W. Short, T. Kessler, R. S. Craxton, S. Letzring, and J. M. Soures, J. Appl. Phys. **66**, 3456 (1989).
[25]S. P. Regan, J. A. Marozas, R. S. Craxton, J. H. Kelly, W. R. Donaldson, P. A. Jaanimagi, D. Jacobs-Perkins, R. L. Keck, T. J. Kessler, D. D. Meyerhofer, T. C. Sangster, W. Seka, V. A. Smalyuk, S. Skupsky, and J. D. Zuegel, J. Opt. Soc. Am. B **22**, 998 (2005).
[26]F. J. Marshall, J. A. Delettrez, R. Epstein, R. Forties, R. L. Keck, J. H. Kelly, P. W. McKenty, S. P. Regan, and L. J. Waxer, Phys. Plasmas **11**, 251 (2004).
[27]INRAD Optics, Northvale, NJ 07647.
[28]D. K. Bradley, P. M. Bell, O. L. Landen, J. D. Kilkenny, and J. Oertel, Rev. Sci. Instrum. **66**, 716 (1995).
[29]J. A. Oertel, T. Archuleta, C. G. Peterson, and F. J. Marshall, Rev. Sci. Instrum. **68**, 789 (1997).
[30]C. Stoeckl, R. Boni, F. Ehrne, C. J. Forrest, V. Yu. Glebov, J. Katz, D. J. Lonobile, J. Magoon, S. P. Regan, M. J. Shoup III, A. Sorce, C. Sorce, T. C. Sangster, and D. Weiner, Rev. Sci. Instrum. **87**, 053501 (2016).
[31]J. Delettrez, R. Epstein, M. C. Richardson, P. A. Jaanimagi, and B. L. Henke, Phys. Rev. A **36**, 3926 (1987).
[32]I. V. Igumenshchev, D. H. Edgell, V. N. Goncharov, J. A. Delettrez, A. V. Maximov, J. F. Myatt, W. Seka, A. Shvydky, S. Skupsky, and C. Stoeckl, Phys. Plasmas **17**, 122708 (2010).
[33]Prism Computational Sciences, Inc., Madison, WI 53711.